UCLA
UCLA Previously Published Works

Title

Metal-to-metal charge transfer for stabilizing high-voltage redox in lithium-rich layered oxide cathodes.

Permalink

https://escholarship.org/uc/item/2hp8q383

Journal

Science Advances, 11(8)

Authors

Kim, Min-Ho
Jang, Haeseong
Lee, Eunryeol
et al.

Publication Date

2025-02-21

DOI

10.1126/sciadv.adt0232

Peer reviewed

eScholarship.org Powered by the California Digital Library
University of California

MATERIALS SCIENCE

Metal-to-metal charge transfer for stabilizing high-voltage redox in lithium-rich layered oxide cathodes

Min-Ho Kim[1]†, Haeseong Jang[2]†, Eunryeol Lee[3,4]†, Jeongwoo Seo[5], Jaehyun Park[6], Ahreum Choi[5], Taewon Kim[7], Myeongjun Choi[5], Euna Kim[5], Yeong Hwa Jung[8], Seok Ju Kang[5], Jaephil Cho[5], Yuzhang Li[1]*, Min Gyu Kim[8]*, Dong-Hwa Seo[9]*, Hyun-Wook Lee[5]*

Copyright © 2025 The Authors, some rights reserved; exclusive licensee American Association for the Advancement of Science. No claim to original U.S. Government Works. Distributed under a Creative Commons Attribution NonCommercial License 4.0 (CC BY-NC).

Apart from conventional redox chemistries, exploring high-voltage anionic redox processes, such as pure oxygen or high-valent transition metal ion redox, poses challenges due to the instability of O nonbonding or O-dominant energy states. These states are associated with destructive behaviors in layered oxide cathodes, including local structural distortion, cationic disordering, and oxygen gas evolution. In this study, we suppress first-cycle voltage hysteresis and irreversible O_2 evolution in Li-rich oxide cathodes through covalency competition induced by the substitution of electropositive groups. We found that the nonequivalent electron distribution within an asymmetric M_A-O-M_B backbone (metal-to-metal charge transfer via oxygen ligands) increases electron density on electronegative transition metal ions, preventing them from reaching unstable oxidation states within an operating voltage range. This phenomenon is observed across diverse transition metal combinations, providing insights into controlling unnecessary oxygen redox activity. Our findings open new avenues for controlling intrinsic redox chemistry and enabling the rational design of high–energy density Li-rich oxide cathodes.

INTRODUCTION

As theoretical specific capacities in conventional layered oxide cathodes are determined by the oxidizable degree of redox-active transition metals (TM) limits, the possibility of incorporating anionic redox chemistry into the charge compensation system has been extensively explored (*1*–*5*). The cumulative cationic and anionic redox processes enable discharge capacities exceeding 250 mAh g^{-1} with a high upper cutoff potential of >4.6 V (*1*, *6*). However, such high-voltage anionic redox, commonly known as oxygen redox (O redox), not only triggers unwanted phenomena (e.g., the first-cycle voltage hysteresis, voltage fading, cationic disordering, and irreversible phase transition) but also intrinsically contain irreversible capacity contribution due to O_2 gas evolution [O^{2-} (lattice) → O_2 (gas) + $2e^-$] (*7*–*9*). These issues notably limit the practical application of oxygen redox in battery materials. Although various strategies, such as superstructure control (*10*–*12*), compositional control (*13*–*15*), phase transformation (*7*, *16*, *17*), and morphological control (*18*–*21*), have been used to address these challenges, they have so far only provided partial solutions, and a comprehensive understanding of the underlying redox mechanisms is still lacking.

Up to date, the emergence of various O redox modeling approaches [including the reductive coupling mechanism (*22*), structure-redox coupling (*3*), reversible molecular O_2 trap (*8*), and delocalized π-redox (*23*)] has provided insights into its potential reversibility. In particular, O redox has generally been understood as the extraction of labile electrons from the Li-O-Li configuration (*2*). This is because, given the orbital orientations of TM t_{2g} orbitals and O 2*p* orbitals in typical Li-rich layered oxides [$xLi_2TMO_3 \cdot (1\text{-}x)LiTMO_2$], it is reasonable to assume that they do not hybridize via sigma (σ) interaction (that is, they cannot form M—O bonds) (Fig. 1A). As a result, both remain isolated as nonbonding states above the O band. However, the new and sometimes conflicting ideas about the mechanism of O redox in battery materials can be difficult to navigate and establish a unified picture of redox chemistry in Li-rich oxides. In this regard, the principle of O redox chemistry needs to be interpreted through a fundamental approach based on scientific rationale.

From a molecular orbital perspective, redox chemistry (and its reversibility) closely correlates with the energy states near the Fermi level (E_F). As shown in Fig. 1B, the hybridization between TM *d* orbitals and O *p* orbitals in Li-rich layered oxides results in energy splitting into antibonding states (M band), bonding states (O band), and nonbonding states. After TM redox is complete, with electrons emitted from the M band, subsequent redox occurs via electrons in the nonbonding states. This explains why high-voltage redox is referred to as O redox, where holes are predominantly located around O ions that are linearly bonded to two Li ions (i.e., Li-O-Li configuration) on OTM_2Li_4 octahedra (no bond forms in the Li-O-Li configuration due to the large energy gap) (*2*). This type of O redox has been considered quasi-reversible because the resultant electron holes do not affect M—O bonding states (O band), even if unstable O-related issues occur (e.g., peroxo-like O—O species and O_2 gas evolution).

Recently, however, the possibility of an additional π-type interaction has been raised between TM t_{2g} states and nonbonding O 2*p* states (O_{NB}), leading to electron holes being delocalized across

[1]Department of Chemical and Biomolecular Engineering, University of California, Los Angeles, Los Angeles, CA 90095, USA. [2]Department of Advanced Materials Engineering, Chung-Ang University, Anseong-si 17546, Republic of Korea. [3]Department of Materials Science and Engineering, University of California Berkeley, Berkeley, CA 94720, USA. [4]Materials Sciences Division, Lawrence Berkely National Laboratory, Berkeley, CA 94720, USA. [5]School of Energy and Chemical Engineering, Ulsan National Institute of Science and Technology (UNIST), Ulsan 44919, Republic of Korea. [6]Department of Chemistry and Biochemistry, The Ohio State University, Columbus, OH 43210, USA. [7]Department of Materials, University of Oxford, Oxford OX13PH, UK. [8]Beamline Research Division, Pohang Accelerator Laboratory (PAL), Pohang-si 37673, Republic of Korea. [9]Department of Materials Science and Engineering, Korea Advanced Institute of Science and Technology (KAIST), Daejeon 34141, Republic of Korea.
*Corresponding author. Email: yuzhangli@g.ucla.edu (Y.L.); mgkim@postech.ac.kr (M.G.K.); dseo@kaist.ac.kr (D.-H.S.); hyunwooklee@unist.ac.kr (H.-W.L.)
†These authors contributed equally to this work.

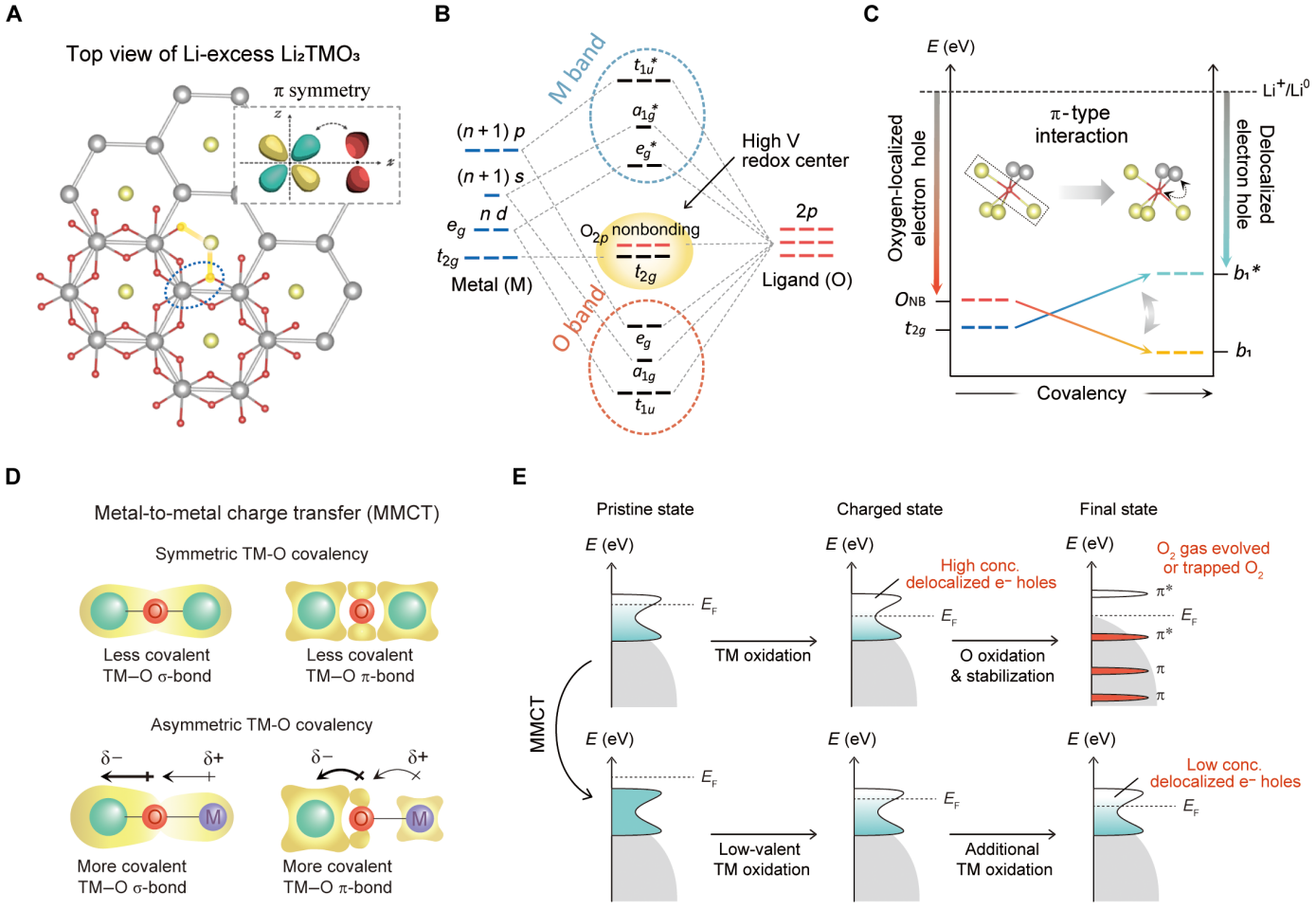

Fig. 1. Band structure of Li-rich oxides and their proposed anionic redox chemistry. (**A**) In-plane cationic ordering of Li/TM within the TM layer; gray, yellow, and red spheres represent TM, Li, and O, respectively. (**B**) Molecular orbital energy diagram in MO_6 octahedron of Li-rich oxides. The σ-type interactions split hybridized energy states into M-dominant band (M band) and O-dominant band, remaining unhybridized TM t_{2g}, and O_{NB}. (**C**) Additional π-type interaction between TM t_{2g} and O_{NB} orbitals varying with the degree of TM—O covalency. Beyond stable M band, low covalency in TM_{3d} (Mn) leads to the electron extraction from O_{NB} states. On the contrary, high covalency in TM_{4d} (Ru) and TM_{5d} (Ir) induces π-type hybridized states with discrete b_1* antibonding states and b_1 bonding states. Here, anionic redox chemistry changes from the oxidation of O_{NB} states to that of deep-lying b_1* states at a high voltage. (**D**) Illustrations of symmetric TM—O covalency in TM-O-TM configuration and proposed asymmetric TM—O covalency in TM-O-M configuration. In contrast to TM-O-TM configuration, asymmetric covalency in TM-O-M induces nonequivalent electron distribution toward more electronegative group. (**E**) The proposed electronic structures induced by metal-to-metal charge transfer (MMCT), contributing to the stabilization of high-voltage redox centers. During high-voltage redox processes, high concentrations of electron holes around the b_1* states can cause redox instability and, thereby, electronic reorganization, potentially leading to the generation of oxygen gas or trapped molecular oxygen. Conversely, an increased electron density around the b_1* states, facilitated by charge transfer, mitigates the electron holes, thereby stabilizing the high-voltage redox chemistry.

TM—O π-bonds (Fig. 1C) (*24*, *25*). This chemistry has been often exploited to explain the redox behavior of high-valent species (*26*, *27*). On the basis of point symmetry, such π-type interaction induces additional b_1/b_1* splitting, which can be further intensified with stronger TM—O covalency (*28*), for example, through shortening the TM—O bond length or with more diffuse *nd* orbitals (e.g., 3*d* Mn, 4*d* Ru, and 5*d* Ir in increasing order) (*29*, *30*). Considering that the reversibility of anionic redox is limited to a critical number of electron holes (localized) per O (*31*), it is plausible that the delocalized electron holes (that is, additional interaction of O_{NB} with TM neighbors) enhance the reversibility of anionic redox chemistry. However, Bruce and colleagues (*25*) revealed that, over time, these delocalized electron holes can condense to form molecular O_2. This suggests that electron delocalization alone cannot prevent irreversible anionic redox, causing well-known degradation phenomena in typical layered cathode materials.

Here, we propose an approach to achieve stable high-voltage redox in Li-rich cathodes by pushing unstable redox couples outside the operating voltage range through the incorporation of an electropositive group to create asymmetric TM—O covalency. We use $Li_{2-x}RuO_3$ (hereafter, LRO) as a simple model system, with 3*d* TM ions (Mn, Co, and Ni) as electropositive substituents, to interpret the effect of nonequivalent electron distribution on high-voltage redox without any interference from the unstable oxygen redox of the Li_2MO_3 phase (*32*). Since LRO is composed of a single metal with strong electronegativity (*33*), it conveniently allows us to identify the structural and electronic changes through the substitution of electropositive 3*d* TM ions. Similar to Li- and Mn-rich layered cathodes, it is

known that LRO with Ru^{4+} (low spin $t_{2g}^4e_g^0$) exhibits TM redox at <4.2 V and O redox at >4.2 V (*34*). The Ru ions in LRO can be destabilized upon persistent charging beyond 4.2 V, and a high concentration of electron holes sufficiently leads to structural and electronic reorganization with structural distortion for the energetic stabilization of cathode materials, giving rise to O_2 gas or trapped O_2 (*8*, *25*). In this study, we used covalency competition between Ru—O and TM_{3d}—O, inducing nonequivalent electron distribution toward electronegative Ru in two ways: through σ-bonds and π-bonds (Fig. 1D). This electron polarization (hereafter referred to as metal-to-metal charge transfer via oxygen ligand) across Ru-O-TM_{3d} not only lowers the oxidation state of Ru by filling its empty t_{2g} states but also intensifies the covalency of Ru—O σ-bonds by sharing more electrons. We demonstrate that both effects improve high-voltage redox chemistry by shifting the operating voltages of multivalent Ru redox (especially high-valent $Ru^{>5+}$ or oxygen-related redox) upward without generating holes at deep-lying O-dominant b_1* state during charging (Fig. 1E). Our findings provide valuable insights into the redox mechanisms of Li-rich cathodes and offer a material design strategy to achieve stable high-voltage redox chemistry, which has not yet been reported in this field.

RESULTS

Structure and electrochemistry of LRO

LRO was synthesized using a conventional solid-state reaction, as detailed in Materials and Methods (*35*). The structure of the synthesized LRO was refined to a layered structure with *C2/c* symmetry, where the TM and Li layers are alternately stacked (fig. S1). The superstructure peaks ranging from 19° to 34° originate from the typical $Li_{1/3}TM_{2/3}$ honeycomb-type ordering in the TM layers. The slight peak asymmetry and broadening are attributed to the presence of defects and stacking faults, similar to those observed in previously reported Ru-based Li-rich cathodes (*34*, *36*).

The voltage profile of LRO during the first cycle is shown in Fig. 2A. The theoretical capacity is estimated to be 164.5 mAh g^{-1}, corresponding to the $Ru^{4+/5+}$ redox reaction (*34*), which involves the extraction of an electron with an opposite spin state on the Ru t_{2g} state (low spin $t_{2g}^4e_g^0$). During the low-voltage $Ru^{4+/5+}$ redox process, LRO exhibits negligible voltage hysteresis (blue curve) on the first cycle. However, if cell voltage reaches an upper cutoff voltage of 4.6 V, then LRO delivers 318.0 mAh g^{-1} (corresponding to 1.93 Li^+ per formula unit) on charge and 299.6 mAh g^{-1} (corresponding to 1.82 Li^+ per formula unit) on discharge and suffers from substantial voltage hysteresis (black curve), accompanied by large amounts of O_2 gas evolution, as confirmed by operando differential electrochemical mass spectroscopy (DEMS) analysis (Fig. 2A, bottom). This indicates that highly charged LRO cannot sustain the resulting delocalized electron holes in Ru—O b_1* states, leading to the decoordination of lattice O from the crystal network. These findings suggest that, after one Li^+ (and e^-) is extracted from LRO, further oxidation of $LiRuO_3$ (low spin $t_{2g}^3e_g^0$) involves electrons from deep-lying hybridized states (O-dominant b_1* states), which are chemically unstable. In contrast to the O_2 gas, CO_2 gas was barely detected during charging up to 4.6 V, indicating that the oxidized products of LRO are likely delocalized electron holes and O-O dimers (peroxo-like species or molecular O_2) rather than highly reactive O radicals.

The instability of high-voltage redox in LRO is further identified through x-ray diffraction (XRD) analysis at various charged states (pristine, 4.15 and 4.6 V) and the discharged state (2.0 V) (Fig. 2B). At 4.15 V, upon the extraction of one Li^+, the main (003) peak corresponding to the *c* axis shifts to the right, indicating a reduced slab size, and new peaks emerge, representing a structural transformation from O3 (monoclinic) to O1 (hexagonal). Beyond 4.6 V, however, the main peak intensity is notably reduced, implying that the layered structure has collapsed during unstable high-voltage redox. The reduction in peak intensity is not fully recovered even after relithiation to 2.0 V, and an irreversible loss of honeycomb ordering (36.8 %) is observed with asymmetric peak broadening (fig. S2). This is mainly attributed to cationic disordering, particularly in-plane Ru migration, which is directly related to the large voltage hysteresis observed during the first cycle. Rietveld refinement confirms that during charging, a portion of the Ru ions prefers Li sites in the Li layer over the TM layer (1.7% at 3.75 V and 2.6% at 4.6 V; fig. S3), consistent with a previous work. Consequently, the loss of honeycomb ordering is expected due to stacking fault–induced incomplete recovery as the migrated Ru ions return to the TM layer.

To understand the unstable high-voltage redox behavior of LRO during the first cycle, we conducted operando x-ray absorption near edge structure (XANES) analysis at the Ru K-edge (Fig. 2, C and D). XANES is a powerful tool for determining the oxidation state and identifying changes in the local structures of target species by detecting multiple scattering events with neighboring atoms (a brief description can be found in fig. S4) (*37*, *38*). The Ru K-edge XANES plot exhibits two distinct white line peaks at around 22,140 eV (denoted as WL1) and 22,150 eV (denoted as WL2) (Fig. 2C) (*39*). During the oxidation from Ru^{4+} to Ru^{5+}, WL1 peak intensity decreases, and WL2 peak intensity increases, resulting in the typical XANES profile for $LiRu^{5+}O_3$ (*39*). Simultaneously, the XANES energy of LRO shifts to higher values, indicating an increase in the Ru oxidation state. However, the rate of energy increase rapidly slows beyond 4.15 V, suggesting that oxidation at high voltages is more associated with delocalized electrons across Ru—O bonds (i.e., Ru—O b_1* redox) rather than with localized electrons near Ru (i.e., Ru redox). This is accompanied by a simultaneous decrease in the intensities of both WL1 and WL2 peaks. This phenomenon can be attributed to reduced electron scattering near the Ru orbitals in the XAFS measurements, likely due to cationic disorder and the loss of oxygen ligands available for scattering. Previously, it was reported (*31*, *40*) that highly oxidized Ru ions ($Ru^{>5+}$) tend to reduce back to Ru^{5+} by pulling electrons from O ligands (a process known as ligand-to-metal charge transfer) associated with enthalpic penalty (*26*), leading to the formation of peroxo-like species with holes around O. In conclusion, we found that charge compensation in LRO at high voltages is predominantly contributed by O (that is, anionic redox), resulting in local structural distortion of RuO_6 octahedra and decoordination of O ligands from the atomic network. This conclusion is further supported by changes observed in the pre-edge region of XANES plots. Note that the pre-edge region provides information on electronic transitions from the core level to unoccupied 4*d*-5*p* hybridized states, which are sensitive to local structural distortions due to the dipole selection rule for forbidden transitions in K-edge spectroscopy (*37*, *39*, *41*). Upon charging to 4.6 V, both XANES spectra (yellow) (Fig. 2C, top) and the difference in XANES intensity (ΔI) between the *n*th spectra (I_n) and the first spectra (I_1) (Fig. 2C, bottom) show clear peak evolution in the pre-edge region (noted as *i*) around 22,120 eV. This indicates that ligand-to-metal charge transfer around Ru triggers configurational asymmetry during oxidation, leading to the formation of peroxo-like O-O species or molecular O_2.

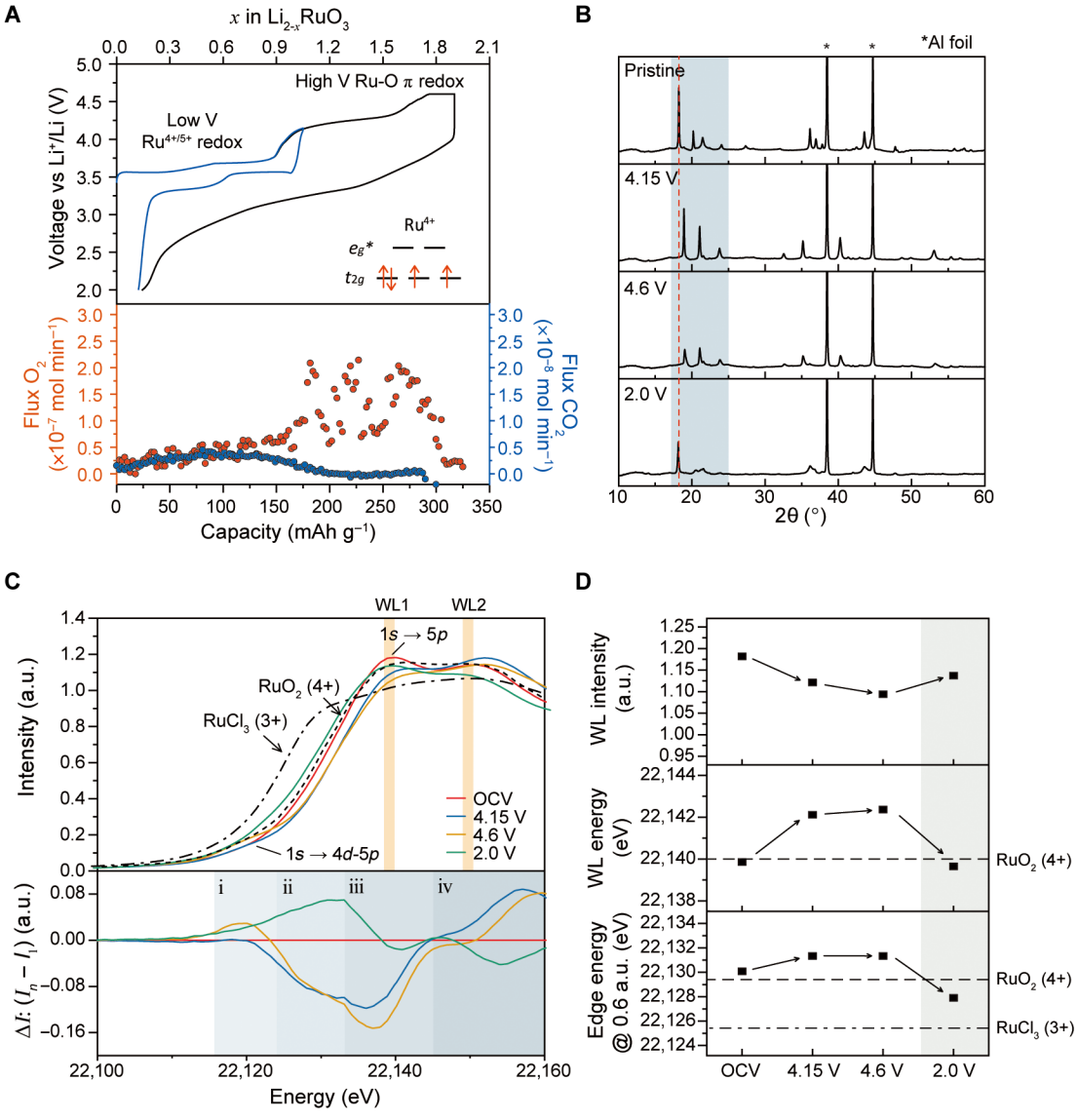

Fig. 2. Electrochemistry of lithium ruthenate (LRO) between 4.6 and 2.0 V. (**A**) Voltage-capacity curves of LRO measured galvanostatically at a C/10 rate between 4.6 and 2.0 V (black) and between 4.0 and 2.0 V (blue), along with operando DEMS showing a substantial amount of oxygen evolution occurring beyond 4.15 V. As electrons are extracted from the Ru t_{2g} states up to 4.15 V (corresponding to the $Ru^{4+/5+}$ redox couple), only a trivial voltage hysteresis is observed. However, beyond 4.15 V, the voltage hysteresis becomes severe, indicating that the atomic structure is modified during deep charging. (**B**) High-resolution synchrotron XRD patterns at various charged states (pristine, 4.15, and 4.6 V) and at the discharged state (2.0 V). Superstructure peaks in the 18° to 25° range are highlighted in the blue box. When the cell voltage reaches 4.15 V, an irreversible structural transformation occurs, accompanied by atomic disordering. (**C** and **D**) Operando Ru K-edge x-ray absorption near edge structure (XANES) spectra (top) and their intensity variations (bottom) during the first cycle. Ru XANES plots have two white line peaks (labeled as WL1 and WL2), which can be used as signatures for Li_2RuO_3 phase by comparing their relative intensities. The evolution of the peak in the pre-edge region (around 22,120 eV, labeled as *i*) indicates local structural distortion of the RuO_6 octahedra. Ru XANES energy, corresponding to variations in oxidation states of Ru during the first cycle, is presented in (D). a.u., arbitrary units.

High-voltage redox stabilized by Ni substitution

To induce metal-to-metal charge transfer toward Ru, we substituted electropositive Ni, which is redox active within the voltage range of 4.6 to 2.0 V. Ni-substituted LRO with varying Ni contents [20, 22, 25, and 50 atomic % (at %) of total TM contents] was synthesized, hereafter referred to as LRO-Ni20, LRO-Ni22, LRO-Ni25, and LRO-Ni50, respectively; $Li_{1.23}Ni_{0.155}Ru_{0.615}O_2$ for LRO-Ni20, $Li_{1.22}Ni_{0.17}Ru_{0.61}O_2$ for LRO-Ni22, $Li_{1.2}Ni_{0.2}Ru_{0.6}O_2$ for LRO-Ni25, and $Li_{1.2}Ni_{0.4}Ru_{0.4}O_2$ for LRO-Ni50 (Supplementary Text 2). These Ni-substituted LRO samples share a similar crystal structure, which fits well with the *C*2/c space group, showing slight peak asymmetry and broadening (Fig. 3A and fig. S6). The *I*(003)/*I*(104) values, which indicate the degree of cationic ordering in the layered structure (*42*, *43*), suggest that Ni substitution somewhat reduces the layered ordering, because Li and Ni atoms are likely to be in the TM layers. In general, it is well-known that Ni atoms tend to occupy Li sites in both Li layers and TM layers, which increases the likelihood of cationic disorder of Li^+/Ni^{2+} (*44*). Among the selected Ni contents, LRO-Ni22 exhibited the most superior layered

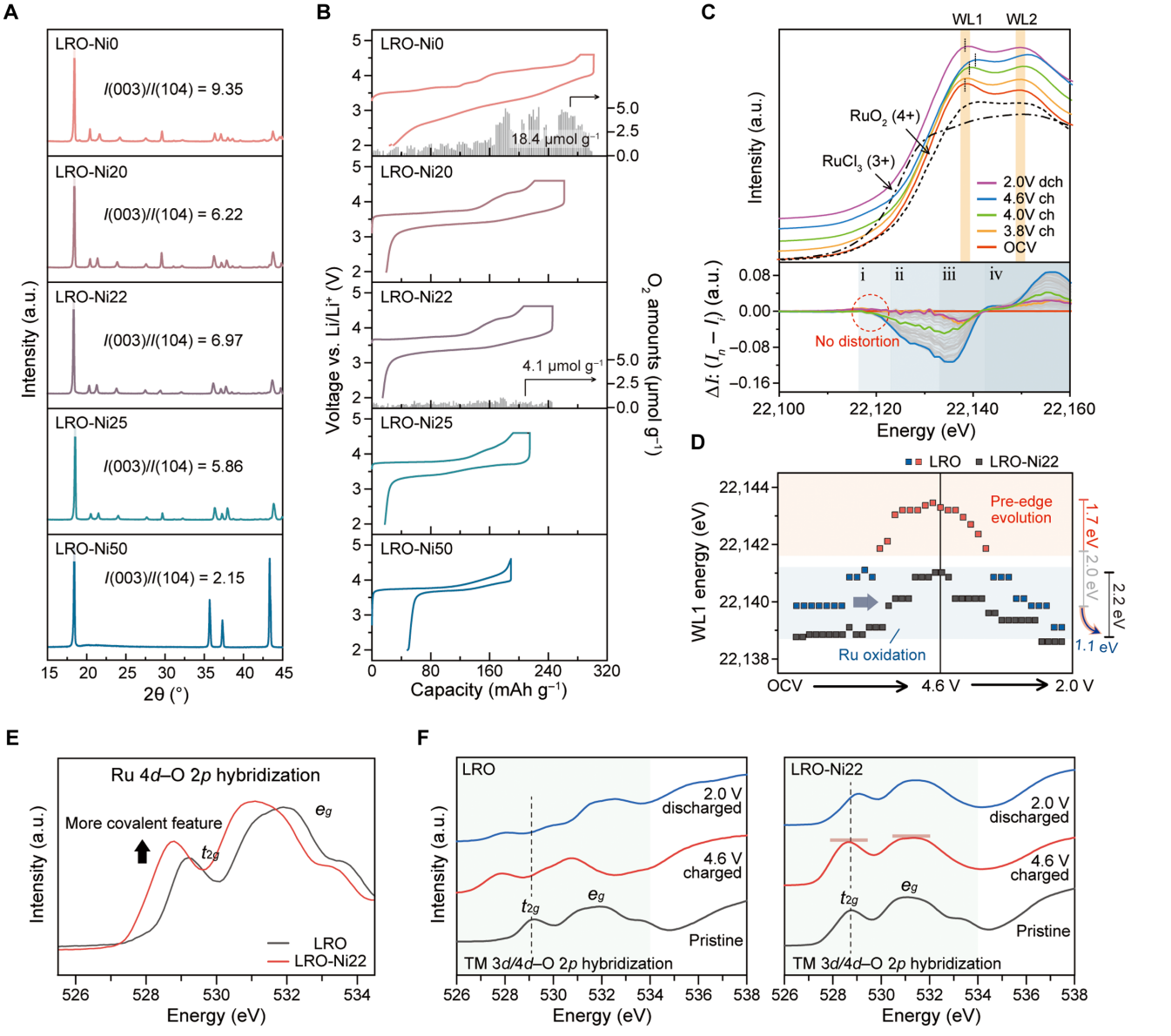

Fig. 3. Structural and electrochemical properties of Ni-substituted lithium ruthenate (LRO). (**A**) XRD patterns of Ni-substituted LRO with various Ni contents (0, 20, 22, 25, and 50 at %, noted as LRO-Ni0, LRO-Ni20, LRO-Ni22, LRO-Ni25, and LRO-Ni50, respectively). The *I*(003)/*I*(104) refers to the degree of layered ordering. (**B**) Voltage-capacity curves of all Ni-substituted LRO at a C-rate of C/10 within the voltage range of 4.6 and 2.0 V. Black bar charts for LRO-Ni0 and LRO-Ni22 indicate the amount of oxygen evolution during charging to 4.6 V. LRO-Ni0 evolves 18.4 μmol g^{-1} of O_2, whereas LRO-Ni22 exhibits only 4.1 μmol^{-1} of O_2, demonstrating its superior redox stability. (**C**) Operando Ru XANES spectra (top) and their intensity variations (bottom) for LRO-Ni22 during the first cycle. In contrast to charged LRO, charged LRO-Ni22 does not exhibit any local structural distortion (red dashed circle), as identified in the pre-edge region (*i*). dch, discharged; ch, charged. (**D**) Comparison of WL1 peak energy variations between LRO and LRO-Ni22 during the first cycle. This confirms that LRO-Ni22 operates with lower Ru oxidation states (shaded in the blue box) than LRO, without reaching the chemically unstable Ru energy range (shaded in the red box). (**E**) Relative covalency of TM—O bonding in LRO (black) and LRO-Ni22 (red) at the pristine state. Larger spectral intensity corresponds to an increased number of electron holes in the Ru 4*d*–O 2*p* hybridized states, indicating stronger bond covalency. (**F**) Variations in spectral intensity for LRO (left) and LRO-Ni22 (right) at different states (pristine, 4.6 V charged, and 2.0 V discharged), illustrating peak shifts and the evolution of Ru—O t_{2g} peaks in intensity.

structure, with the highest *I*(003)/*I*(104) value. Its electrochemical behavior shows that Coulombic efficiencies closely correlate with *I*(003)/*I*(104) values, leading us to select LRO-Ni22 as the representative Ni-substituted LRO.

Notably, LRO-Ni22 delivers 262.2 mAh g^{-1} (corresponding to 1.1 Li^+) on charge and 231.1 mAh g^{-1} (corresponding to 0.97 Li^+) on discharge in the voltage range of 4.6 to 2.0 V, exceeding its theoretical capacity of 227.1 mAh g^{-1} (corresponding to 0.95 Li^+), calculated on the basis of $Ni^{2+/4+}$ and $Ru^{4+/5+}$ redox. Despite its unusually high delivery capacity, DEMS results unexpectedly confirm that irreversible O_2 gas evolution was notably mitigated in LRO-Ni22, compared to LRO. As a result, the electrochemical stability of LRO-Ni22 was greatly enhanced through Ni substitution, consistent with XRD results showing only a 10.8% loss in superstructure across a wide operating voltage

range, compared to a 36.8% loss in LRO (fig. S7). This finding indicates that irreversible cationic disordering is effectively suppressed in LRO-Ni22.

Ru XANES data further clarify that charge compensation in LRO-Ni22 is influenced by Ni substitution (Fig. 3, C and D). When comparing the XANES energies for $RuCl_3$ (Ru^{3+}) and RuO_2 (Ru^{4+}), the Ru oxidation state in pristine LRO-Ni22 is found to be between +3 and +4 (Fig. 3C, red curve), with the Ru WL energy in LRO-Ni22 at 22,139 eV, slightly lower than in LRO (22,140 eV). This suggests that Ru ions are reduced through Ni substitution, drawing electrons from neighboring atoms. The Ni XANES plot for pristine LRO-Ni22 is slightly shifted toward higher energy compared to Ni^{2+} in NiO (fig. S11) (*13*), indicating a lower charge density than that in NiO. On the basis of this observation, we conclude that electrons tend to move from Ni to Ru via the O ligand in the Ru-O-Ni atomic configuration, a well-known phenomenon in binary metal compound catalysts (*45*, *46*).

In the meantime, assuming a linear relationship between formal oxidation states and WL energy (*47*–*49*), we found that Ni ions deliver only 48.8 mAh g^{-1} by oxidizing from +2.2 to +3.4, while Ru ions contribute 212.0 mAh g^{-1} (corresponding to 1.46 e^- per Ru ion) by oxidizing from +3.5 to +4.96. Although Ru ions provide more electrons than expected (1.0 e^-) during continuous oxidation to 4.6 V, no typical signature of local atomic distortion is detected in the pre-edge region (Fig. 3C, bottom), in stark contrast to the LRO case. This consistent observation suggests that the high-voltage redox of LRO-Ni22 is both chemically and structurally stable.

Overall, as shown in Fig. 3D, the change in oxidation state of Ru in LRO-Ni22 occurs within its chemically stable regime (blue shaded area). As previously mentioned, charge compensation in LRO during charging to 4.6V involves both a stable $Ru^{4+/5+}$ redox (WL1 energy shift of 2.0 eV) and an unstable $Ru^{>5+}$-O redox (WL1 energy shift of 1.7 eV). However, the WL1 energy of LRO-Ni22 is 1.1 eV lower than that of LRO in the pristine state, and its energy shift begins at a higher voltage compared to LRO. This suggests that the Ru redox potential in LRO-Ni22 is shifted to a higher voltage than in LRO, although its Ru oxidation state is lower. Furthermore, the WL1 energy of LRO-Ni22 does not reach the unstable regime (red shaded area), where the pre-edge peak evolves in LRO within the same voltage range.

In addition, we analyzed the soft O K-edge x-ray absorption spectroscopy (XAS) to examine Ru—O bond covalency in LRO and LRO-Ni22. The O XAS technique has emerged as an effective method for quantitatively probing the O 2*p* characters (e.g., electronic structure) due to metal-oxygen orbital mixing, wherein the oxygen 1s core electron is excited to its lowest empty states (*50*, *51*). In general, the integrated intensity of the pre-edge peak (at 529 eV for Ru t_{2g}-O_{2p} and at 532 eV for Ru e_g-O_{2p}) is closely associated with the degree of TM—O covalency, as stronger covalency results in more unoccupied hybridized states between metal and oxygen (*13*). As shown in Fig. 3E, covalency in LRO-Ni22 is found to be stronger than in LRO, providing strong evidence that Ni substitution intensifies Ru—O covalency. Also, we demonstrate that high-voltage redox in LRO-Ni22 forms electron holes in the Ru t_{2g}-O_{2p} hybridized states, while redox in LRO involves reconstruction of electronic structures and shifts in spectral energy, likely due to conformational changes in RuO_6 local structures (Fig. 3F). On the basis of these synchrotron x-ray analysis results, we confirmed that the Ni substitution effectively stabilizes the electrochemistry of LRO-Ni22 at high voltages by enhancing Ru—O covalency.

Redox potential shifts induced by 3*d* TM substitution (Mn, Co, and Ni)

To further investigate this phenomenon, we generalized metal-to-metal charge transfer by incorporating Mn, Co, and Ni into LRO (denoted as LRO-Mn22, LRO-Co22, and LRO-Ni22, respectively). Figure 4A shows their voltage profiles with respect to normalized capacity. Notably, the TM-substituted samples consistently exhibit increased redox potentials compared to LRO. This trend is also evident in the dQ dV^{-1} plots (fig. S14). In the early stages of charging, the redox onset potentials for 3*d* TM-substituted samples consistently shift upward relative to the LRO voltage profile (Fig. 4A, inset), indicating that the electronic structure of the samples is intrinsically altered by the 3*d* TM substitution. Furthermore, all substituted samples exhibit reduced voltage hysteresis compared to LRO, suggesting the suppression of cationic disorder and local structural distortion (*8*). The electrochemical characteristics of the samples (e.g., voltage profiles, Coulombic efficiency, cyclability, etc.) vary according to the distinct redox chemistries of the substituted TM ions (see Supplementary Text 4). Our computational results demonstrate that compositional modifications, including doping and substitution, alter the most stable phases for each sample depending on state-of-charge (SOC), ultimately affecting the voltage profiles (figs. S15 and S16). Nevertheless, the DEMS data consistently confirm that the high-voltage redox stability induced by TM substitution effectively suppresses oxygen evolution, regardless of the specific 3*d* TM substituted (Fig. 4B).

Ru XANES results provide insightful information on the electronic reorganization resulting from the substitution (Fig. 4C). When 3*d* TM is substituted, the Ru oxidation states decrease in the following order: LRO > LRO-Mn > LRO-Ni > LRO-Co. We hypothesize that this trend in electron density around Ru is influenced by (i) the electronegativity and (ii) the electron occupancy in the t_{2g} state of 3*d* TM substituents, dictated by the Pauli's exclusion rule (see fig. S18) (*52*). As TM ions are integrated into the atomic structure of the cathode materials, their *d* orbitals hybridize with the *p* orbitals of O ligands, forming bonds. In the linear configuration of Ru-O-M_{3d}, it is reasonable to infer that the strong electronegative nature of Ru allows it to share more electrons with the oxygen center than the electropositive 3*d* TM does. This may lead to an increase in bond covalency between Ru and O, a phenomenon already known as the inductive effect (*53*, *54*). The inductive effect refers to a local change in electron density within covalent bonds due to the presence of electropositive or electronegative groups, resulting in a permanent dipole in the bond. The more electrons the TM ions share with O ligands, the stronger the TM—O interactions become. Considering that thermodynamic redox potential is dependent on the interaction between M *nd* orbitals and O *p* orbitals according to ligand field theory (*55*), their redox potentials, particularly in terms of the lowest unoccupied molecular orbital level (i.e., fermi level), can be influenced by the electron occupancy in the t_{2g} state.

In this regard, let us consider that more partial electrons are located around down-spin t_{2g} states on Ru ions by drawing electrons from the opposite TM_{3d}—O bonds (Fig. 4D). The resultant strong interaction between Ru *d* orbitals and O *p* orbitals in an octahedral complex leads to greater splitting of *d* orbitals into two sets: e_g orbitals and t_{2g} orbitals, due to increased repulsion between electrons on the Ru e_g states and on O *p* orbitals in terms of σ interaction. Simultaneously, t_{2g} states on which the electrons are populated will be lower in energy, thereby increasing the redox potential. As mentioned earlier, this intensified

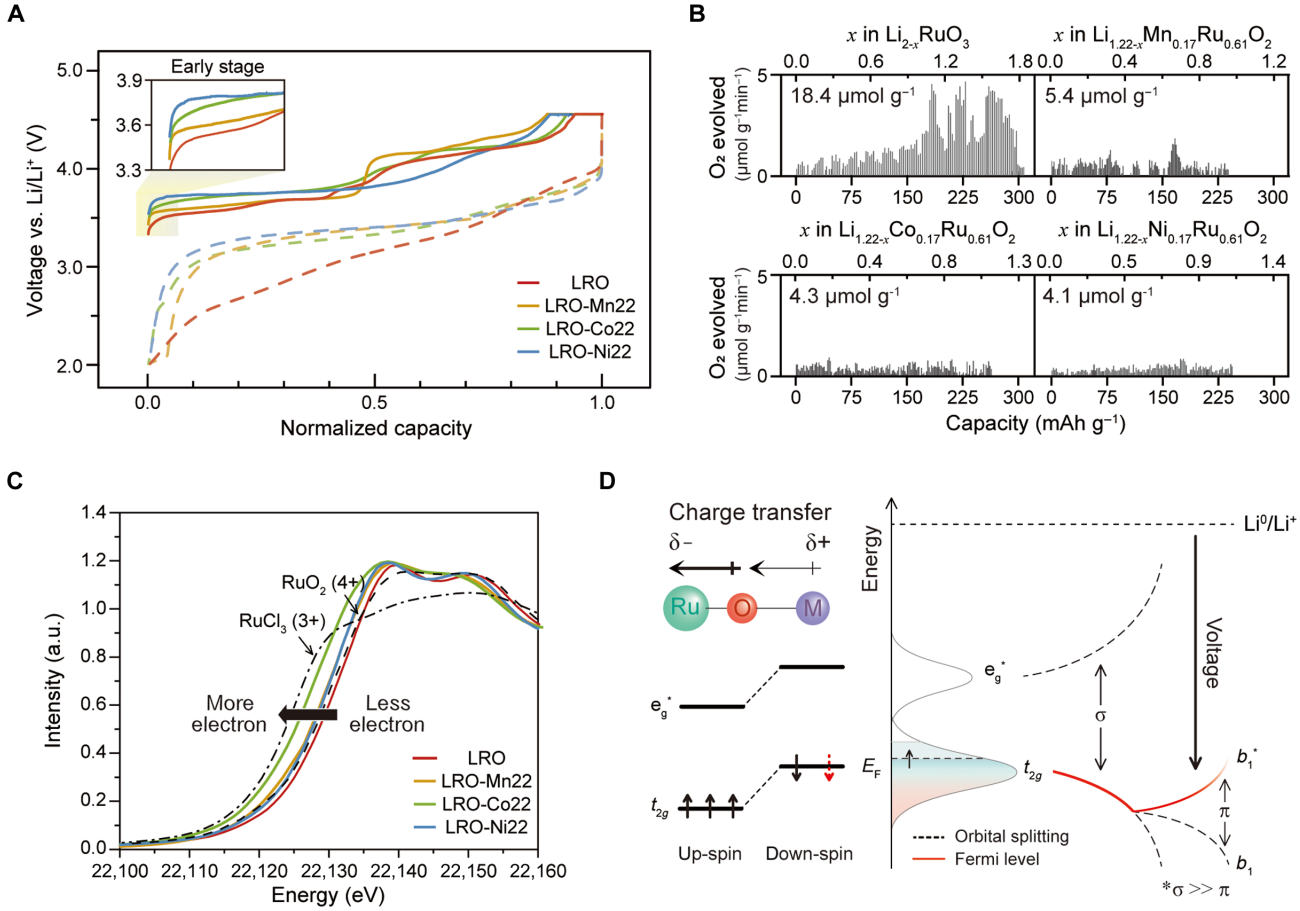

Fig. 4. Correlating redox voltage shifts with metal-to-metal charge transfer. (**A**) Normalized voltage profiles within the voltage range of 4.6 and 2.0 V in TM-substituted LRO (TM = Mn, Co, and Ni). (**B**) Analysis of the amounts of oxygen evolution in LRO and all the TM-substituted LRO during charging to 4.6 V. Regardless of which 3*d* TM is substituted, oxygen evolution is effectively suppressed compared to LRO. (**C**) Variations in the electronic structures of Ru, induced by metal-to-metal charge transfer toward Ru. The Ru oxidation states in all TM-substituted LRO are lower than in LRO, indicating more electrons around Ru ions. This is highly correlated with the relative electronegativity of Ru compared to the 3*d* TM and bond order. (**D**) Proposed principles for redox voltage shifts depending on 3*d* TM incorporation. When additional electrons populate the Ru t_{2g} states, the Ru—O bond covalency becomes stronger, inducing larger orbital splitting via σ interaction through the inductive effect. This accompanies additional π interaction, which determines the final cathode potentials. In general, σ interaction is much stronger than π interaction, indicating that relative electronegativity plays a critical role in influencing charge transfer.

σ interaction is accompanied by stronger π interaction, resulting in additional splitting of b_1 and b_1* states. Although this additional splitting is influenced by the number of outmost electrons and plays a role in determining relative potential shifts depending on the substituted ions, all 3*d* TM-substituted samples commonly exhibit increased redox potentials than LRO because the intensity of splitting in σ bond is much stronger than in π bond. In other words, charge transfer via σ interaction is more critical for increasing oxygen redox potential than π interaction, even if outmost electrons occupy the t_{2g} state and interact with O ligands via π orientation.

Previously, it was reported (*36*) that no anionic redox activity was observed in $Li_{1.2}Ni_{0.2}Ru_{0.6}O_2$, as confirmed by resonant inelastic x-ray scattering. The authors explained that this might be attributed to insufficient Li content to allow all O atoms to exist in a Li-O-Li configuration, although this explanation remains inconclusive. In this work, we approach this phenomenon in terms of the metal-to-metal charge transfer, induced by covalency competition in the Ru-O-TM_{3d}. This approach enables us to extend the concept across diverse TM combinations and clarify the fundamental principles for suppressing unnecessary oxygen redox activity. In conclusion, incorporating electropositive TM into LRO not only intensifies TM—O bond covalency but also increases the potential of the redox couples, which is beneficial for high–energy density cathodes.

Local structural evolution within 4.6 to 2.0 V

So far, many previous papers (*3*, *56*, *57*) have reported on the correlation between redox chemistry and structural transformation in Li-rich oxides. To further understand the different high-voltage redox behaviors of LRO-Ni22 compared to LRO, we measured the local structural evolution during battery operation using operando extended x-ray absorption fine structure (EXAFS) at the Ru and Ni K-edges. The radial distribution function (RDF) of Fourier-transformed (FT) k^3-weighted EXAFS provides local structural information for specific TM ions, including atomic disordering, coordination numbers, and interatomic distances. In three-dimensional (3D) contour maps of RDF (Fig. 5A), a peak at ~1.6 Å corresponds to the distance between

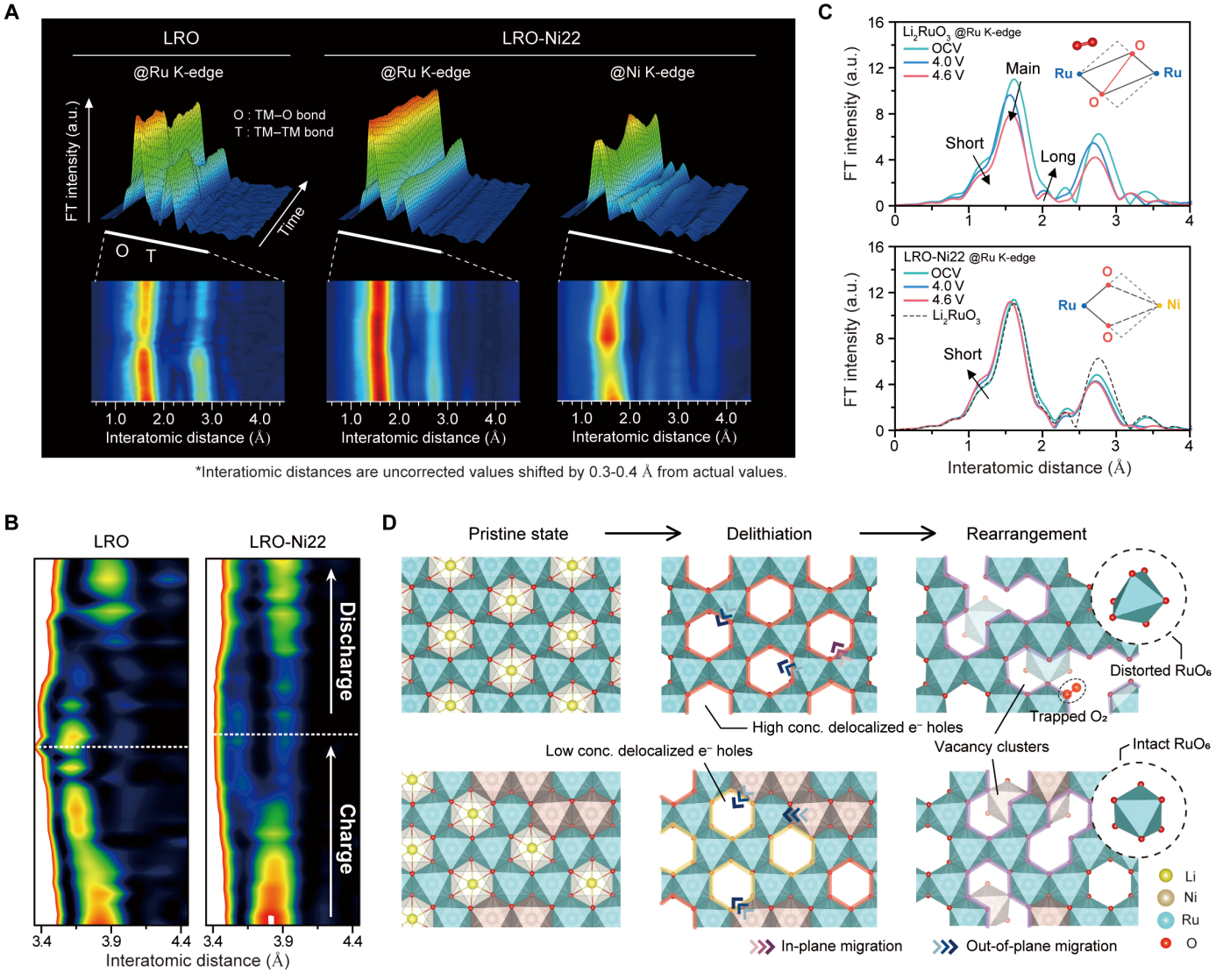

Fig. 5. Atomic structure evolution and electronic structure in LRO and LRO-Ni22. (**A**) 3D and 2D contour maps obtained from operando EXAFS oscillations during the first cycle; the FT peak positions of TM-O (denoted as O) and TM-TM (denoted as T) are ~1.6 and ~2.7 Å, respectively. Note that interatomic distances shown in the figure are uncorrected values, shifted by 0.3 to 0.4 Å from actual values. (**B**) 2D contour map shows out-of-plane cationic migration during the first cycle, where the peak evolution at ~3.6 Å represents Ni migration toward the Li layer relative to immobilized Ru. Since Ru atoms in LRO barely migrate to the Li layer, the peak splitting is expected to occur due to in-plane migration and structural distortion. (**C**) Ru EXAFS spectra of LRO (top) and LRO-Ni22 (bottom); the O peak is subdivided into three peaks corresponding to short TM—O bonding (~1.4 Å), main TM—O bonding (~1.6 Å), and long TM—O bonding (~2.0 Å). The spectral variation in the Ru K-edge spectra of LRO is quite large due to severe structural distortion in deeply charged states. In contrast, the Ru K-edge spectra of LRO-Ni22 remain mostly unchanged, except for a slight evolution of the short peak, which corresponds to the Ru═O double bond length. (**D**) The proposed redox behaviors of LRO and LRO-Ni22, correlated with local structural transformation and atomic migration. The structure of charged LRO degrades due to large vacancy clusters and local structural distortion of the RuO_6 octahedra. However, incorporating Ni effectively suppresses structural degradation, even in deeply charged states at high voltage regimes, through active Ni migration without affecting Ru atoms.

target Ru atoms and the nearest O atoms in the first coordination shell (denoted as O), and a peak at ~2.7 Å corresponds to that of the nearest TM atoms in the second coordination shell (denoted as T) (*13*). In the Ru EXAFS of LRO (Fig. 5A, left), the intensity of the O peak persistently decreases during charging, with a marked loss observed at the end of the charge. Although this intensity partially recovers upon discharge (perhaps due to the recovery of cationic disordering), the partially irreversible change suggests that irreversible O loss occurs due to gas evolution. This unwanted O loss leads to cationic disordering, as evidenced by the simultaneous decrease in the T peak. This observation is consistent with the Ru XANES results, which show the evolution of a pre-edge peak during oxidation, demonstrating local structural distortion of RuO_6. In stark contrast, no appreciable change in peak intensity is detected in the Ru EXAFS of LRO-Ni22 (Fig. 5A, middle), indicating that both the loss of O ions coordinating Ru and the local structural distortion of RuO_6 octahedra do not occur during the first cycle. Instead, we observed active Ni migration within the crystal structure in the Ni EXAFS of LRO-Ni22 (Fig. 5A, right). Upon charging, the intensity of the Ni-O peak initially decreases and then increases again and repeats during discharge. Given that the intensity

correlates with the coordination number, we infer that Ni migrates through adjacent tetrahedral sites along its thermodynamically preferential routes (*58*). This is further supported by the 2D contour maps of Ru EXAFS of LRO and LRO-Ni22 (Fig. 5B). Typically, a peak at ~3.9 Å (one of the TM-TM peaks) splits into ~3.6 and ~4.0 Å in LRO and LRO-Ni22, implying TM migration. Although severe RuO_6 distortion hinders precise interpretation in LRO, the peak evolution at ~3.6 Å in LRO-Ni22 suggests out-of-plane Ni migration toward the Li layer [from O_h in the TM layer → T_d in the Li layer (intermediate) → O_h in the Li layer on charge] (fig. S19 and Supplementary Text 5).

However, despite the active migration of Ni atoms within the crystal structure, changes in Ru—O bonds are not appreciable. Rather, the movement of Ni atoms appears to create enough space to release accumulated stress around the Ru local structure. This is evident in the Ru—O bond length region in Fig. 5C. As LRO is delithiated, the Ru local structure in LRO becomes markedly distorted (Fig. 5C, top). Notably, after charging above 4.0 V, both the decrease in FT intensity and Ru—O peak splitting are prominent, clarifying that the redox chemistry of Ru beyond an oxidation state of +5 is unstable. In stark contrast, the Ru local structure in LRO-Ni22 remains well-maintained up to 4.6 V (Fig. 5C, bottom). The only change observed is a shortening of the Ru—O bond, as identified by the peak shift toward a shorter Ru—O interatomic distance. We believe that the stabilization of local structural transformation is due to pushing unstable Ru redox out of the operating voltage range by incorporating the inductive effect, thereby achieving both chemical and structural stability in redox behavior.

Figure 5D illustrates the expected redox behaviors of LRO and LRO-Ni22, correlated with local structural transformation and atomic migration. As discussed earlier, Ru redox in LRO is accompanied by active in-plane Ru migration, a common phenomenon in most layered cathode materials. Recently, it was proposed that the formation of vacancy clusters with sizes longer than four atoms in TM layers following delithiation and relaxation traps molecular O_2 within the structure (*59*). This phenomenon is correlated with a voltage slope during discharging, attributed to disordered TM layers, leading to structural instability that degrades redox stability. On the other hand, we propose that incorporating electropositive TM can modulate the potentials of redox couples and eliminate unwanted redox couples within the desired operating voltage window. Specifically, we find that this approach not only stabilizes high-voltage redox chemistry but also suppresses local structural transformations around Ru, the main redox center during high-voltage redox.

We additionally analyzed and plotted the projected density of states (pDOS) and corresponding isosurface of the charge density to capture the hole states in highly charged LRO and LRO-Ni22 (Fig. 6). Note that the model structures for the highly charged samples were determined by removing Li atoms until the oxidation state of Ru reached +5. Although in both pristine samples, electrons are identically extracted from Ru-dominant orbitals during the initial oxidation (Fig. 6, A and B), Ru in LRO-Ni22 contributes more strongly to the valence states around the Fermi level (E_F) (Fig. 6B), suggesting that Ni substitution induces high polarity in the Ru-O-Ni configuration compared to the Ru-O-Ru configuration, particularly with a higher charge density around Ru ions. This polarity reasonably affects the energy levels in the highly charged state. In the charged state with Ru^{5+}, energy states just below E_F in charged LRO transform into O-dominant b_1* states (Fig. 6, C and D), whereas those in charged LRO-Ni22 remain Ru-dominant states (Fig. 6D). The origin of this difference in energy states can be identified by visualizing the charge density around the oxygen ions for the energy range corresponding to the subsequent oxidation after reaching Ru^{5+} (Fig. 6, E and F). As seen in the isosurface plots, the charge density near E_F is widely distributed across the Ru center and O ligands in charged LRO (Fig. 6E), meaning that the O *p* orbitals contribute to further oxidation beyond Ru^{5+} (i.e., a kind of anionic redox). In stark contrast, the charge density in charged LRO-Ni22 still lies around the Ru center, resembling the t_{2g} state of *d* orbitals (i.e., cationic redox) (Fig. 6F). In other words, the high-voltage redox of LRO-Ni22 induces Ru-localized electron holes, whereas LRO exhibits delocalized electron holes between Ru and O. It was recently reported that this delocalized electron hole easily transforms into molecular O_2 during relaxation. Therefore, inducing multivalent TM redox (or cationic TM—O redox), rather than pure O redox, is beneficial for high–energy density cathode materials, as it enhances electrochemical performance, with superior capacity retention of 92.5% over 50 cycles at high temperature of 60°C (compared to 65.6% for LRO) and a reduced voltage decay of 0.05 V (versus 0.30 V for LRO) (figs. S20 to S23). It also maintains structural integrity during repeated cycles, even under harsh conditions (figs. S24 and S25).

DISCUSSION

This study highlights an insightful approach to stabilizing high-voltage redox chemistry in Li-rich layered oxide cathodes by leveraging the concept of electronegativity. By incorporating electropositive TMs, such as Ni, Co, and Mn, the research successfully modulates the redox voltage of unstable redox couples playing anionic redox, effectively shifting them outside the operating voltage range. This approach reduces the occurrence of irreversible oxygen redox and cationic disordering, common issues that compromise the stability of cathode materials. The study reveals that metal-to-metal charge transfer via oxygen ligands not only elevates the Ru redox potential but also suppresses the formation of harmful oxygen species. These findings emphasize the role of electronegativity in controlling redox behavior and present a promising strategy for developing high–energy density cathodes with enhanced electrochemical stability, paving the way for more durable and efficient battery technologies.

MATERIALS AND METHODS

Sample preparation

LRO, LRO-Ni, LRO-Mn, and LRO-Co were prepared by using stoichiometric amounts of Li_2CO_3, RuO_2, $Ni(OH)_2$, $MnCO_3$, and $Co(NO_3)_2{\cdot}6H_2O$ as precursors. A 10 wt % excess of Li_2CO_3 was used to compensate the lithium evaporation during high temperature synthesis. Mixed powder was heat treated at 650°C for 6 hours and 950°C for 12 hours at a ramp rate of 2°C/min in ambient atmosphere, followed by an intermediate grinding process and further heating at 1050°C for 12 hours, except for LRO. Subsequently, the furnace was cooled to room temperature.

Electrochemical characterizations

All electrochemical evaluations in this work were performed by using 2032 coin-type cells under the same conditions on each material. Electrodes were prepared by mixing 80 wt % active material, 10 wt % carbon black, and 10 wt % polytetrafluoroethylene binder dissolved in *N*-methyl-2-pyrrolidone. The obtained slurry was casted on

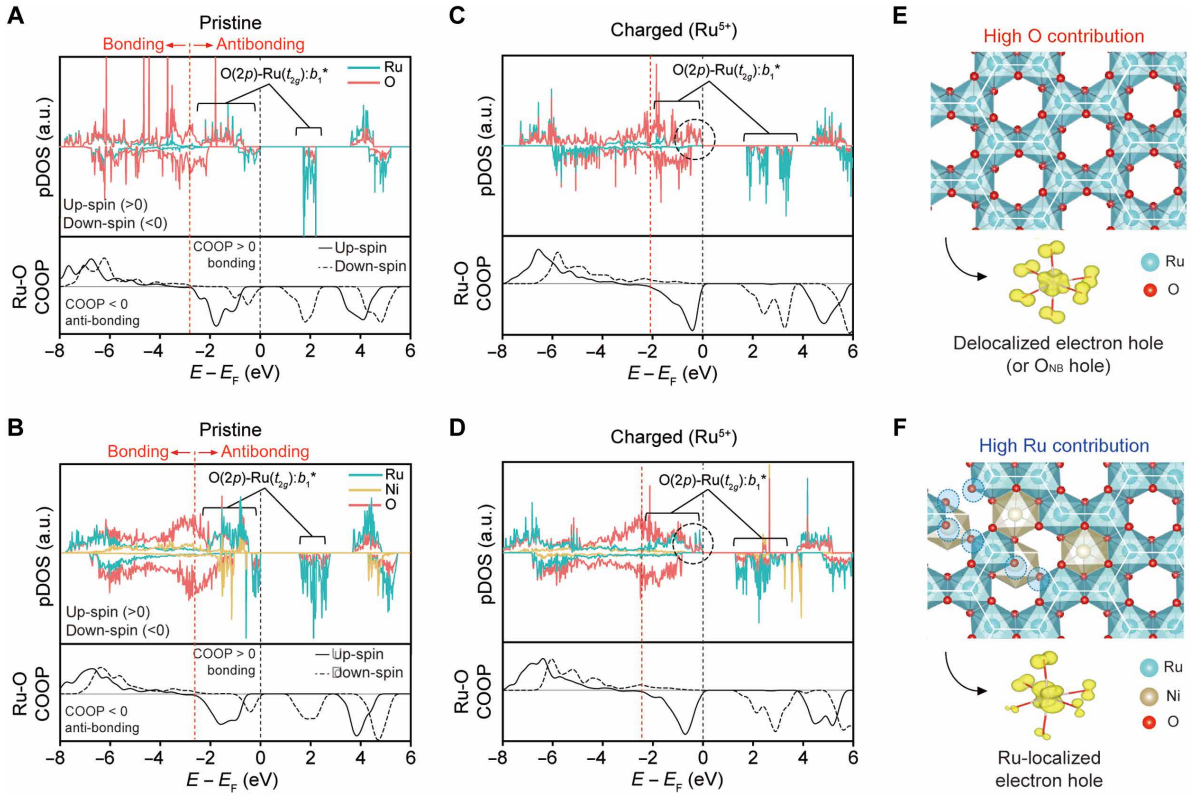

Fig. 6. Calculated electronic structure for LRO and LRO-Ni22. (**A** to **D**) pDOS and crystal orbital overlap population (COOP) plots from DFT calculations for LRO [(A) and (C)] and LRO-Ni22 [(B) and (D)] in both pristine state and charged state with Ru oxidation state of +5. These plots demonstrate that the contribution of Ru to the electron density around the Fermi level is much higher in LRO-Ni22 than in LRO, indicating that the redox behavior of LRO-Ni22 is dominated by Ru rather than O, even in highly charged states. (**E** and **F**) The isosurface of the electron density for following oxidation of LRO (E) and LRO-Ni22 (F) after reaching Ru^{5+}. This clarifies that the high-voltage redox couple in LRO is related to the Ru—O hybridized state, leaving a delocalized electron hole between Ru and O. In contrast, in LRO-Ni22, the electron hole remains close to Ru, indicating that its high-voltage redox behavior is primarily due to Ru oxidation.

aluminum foil using a doctor blade and then dried under vacuum at 120°C for 2 hours. Electrochemical cells were assembled in an argon-filled glove box with Li metal as the counter and reference electrodes. The electrolytes with a composition of 1 M $LiPF_6$ in ethylene carbonate/ethyl methyl carbonate/dimethyl carbonate in a volume ratio of 3:4:3 were used. As a separator, trilayer microporous PP/PE/PP (Celgard, 2325) was used. Electrochemical evaluations were carried out between 4.6 and 2.0 V at 0.1 C-rate for checking the voltage profile and analyzing gas evolution. Cycling performances were tested within the identical voltage range at 0.5 C-rate at room temperature and high temperature (60°C).

Operando XAS analysis

Operando XAS data were collected on the BL10C beamline wide extended x-ray absorption fine structure (WEXAFS) at the Pohang light source (PLS-II) with top-up mode operation under a ring current of 250 mA at 3.0 GeV. Monochromatic x-ray beams were obtained with a liquid nitrogen–cooled double-crystal monochromator (Bruker ASC) with available in situ exchange in vacuum between a Si (111) and Si (311) crystal pair. The Si (111) crystal pair was used for TM K-edge XAS measurements. For operando XAS measurements, pouch-type half-cells were assembled with a counter electrode of Li-metal foil in a dry room, in transmittance mode using N_2 gas–filled ionization chambers (IC-SPEC, FMB Oxford) for the incident and transmitted x-ray photons. To eliminate higher-order harmonic contaminations, we detuned the incident x-ray intensity as reducing by ~30%. With reference TM foils placed in front of the third ion chamber, energy calibration processes were conducted for each XAS measurement. The XAS spectra for all TMs were obtained with a scanning time of 20 to 30 min for one spectrum. Using 0.2 C-rate of charging and discharging, 25 to 35 scans of XAS spectra for each TM were conducted to acquire reliable electronic/crystalline structures. On the basis of the standard XAS analysis procedure, the reductions of spectra data were performed into the normalized XANES and FT RDFs. AUTOBK and FEFFIT modules in UWXAFS package were used to obtain the k^3-weighted TM K-edge EXAFS spectra, $k^3\chi(k)$, with the removal of background and the normalization processes on the edge jump. The $k^3\chi(k)$ spectra were FT in the k range between 2.5 and 12.0 $Å^{-1}$. A difference of 0.3 to 0.5 Å between actual interatomic distances and observation values of RDFs exists because phase correction was not conducted.

Synchrotron XRD analysis

Synchrotron XRD for each electrode with the different SOC during the first cycle was measured from 10° to 120° at 0.02° $step^{-1}$ (10 s for one step) using 9B beamline of the Pohang Accelerator Laboratory for observing phase transition.

Material characterization

The chemical compositions of the cathode material were determined by inductively coupled plasma optical emission spectrometry (Varian 700-ES, Varian Inc.). Operando DEMS analysis was conducted on Swagelok-type cells between 2.0 and 4.6 V (versus Li/Li^+). To detect the dissolved TMs toward anode side, time-of-flight–secondary ion mass spectrometry (TOF-SIMS) mapping (model TOF-SIMS 5, ION-TOF GmbH) was conducted for cycled graphite electrodes, paired with our samples. The analysis chamber was maintained in ultrahigh vacuum at a pressure below 5.0×10^{-10} torr. All detected secondary ions of interest had a mass resolution >10,000.

Density functional calculation

Spin-polarized density functional theory (DFT) calculations were performed using Vienna Ab initio Simulation Package (*60*). The generalized gradient approximation (GGA) with the Perdew-Burke-Ernzerhof functionals (*61*) was used to describe the exchange-correlation potentials. Also, the projector-augmented wave method was used. For a correction of self-interaction error in the *d* orbital states of TM ion, the Hubbard *U* correlations were adopted ($U = 4.0$ and 6.2 for Ru and Ni, respectively). All DFT calculations used a plane wave basis set with an energy cutoff of 520 eV. The atomic position, cell shape, and volume of the structures are fully relaxed (ISIF = 3) until the residual forces on the cell are smaller than 0.05 eV $Å^{-1}$ for all cases. The method to prepare the structures of Li_2RuO_3 and $Li_{1.22}Ni_{0.17}Ru_{0.61}O_2$ and further computational details are provided in Supplementary Text 1. Also, we applied GGA + *U* calculation to evaluate the lowest formation energies of various compositions. The 30 lowest electrostatic energy configurations of Li ions determined using the Ewald summation technique were used for ab initio geometry optimizations at each composition.

The relative stability ΔE_f (electron volts/formula unit) of polymorphs at each Li composition x was evaluated by

$$\Delta E_f = E\left(Li_{2-2x}RuO_3\right) - xE\left(RuO_3\right) - (1-x)E\left(Li_2RuO_3\right) \text{ for LRO}$$

and

$$\Delta E_f = E\left(Li_{1.875-1.875x}Ru_{0.875}TM_{0.25}O_3\right) - xE\left(Ru_{0.875}TM_{0.25}O_3\right) - (1-x)E\left(Li_{1.875}Ru_{0.875}TM_{0.25}O_3\right)$$

for TM (e.g., Mn, Co, and Ni)–substituted LRO, where E is the calculated total energy for a given structure.

The average voltage (V) versus Li/Li^+ was calculated as

$$V = -\left[E\left(Li_{2-2x'}RuO_3\right) - \left(x'-x\right)E(Li) - E\left(Li_{2-2x}RuO_3\right)\right] / \left(x'-x\right) \text{ for LRO}$$

and

$$V = -[E(Li_{1.875-1.875x'}Ru_{0.875}TM_{0.25}O_3) - (x'-x)E(Li) - E(Li_{1.875-1.875x}Ru_{0.875}TM_{0.25}O_3)]/(x'-x)$$

for TM (e.g., Mn, Co, and Ni)–doped Ru oxides, where E is the calculated total energy for a given structure, and x' and x are the Li composition before and after the lithium extraction from the host structure, respectively.

Supplementary Materials

This PDF file includes:

Supplementary Text
Figs. S1 to S25
Tables S1 and S2
References

REFERENCES AND NOTES

1. G. Assat, J.-M. Tarascon, Fundamental understanding and practical challenges of anionic redox activity in Li-ion batteries. *Nat. Energy* **3**, 373–386 (2018).
2. D.-H. Seo, J. Lee, A. Urban, R. Malik, S. Kang, G. Ceder, The structural and chemical origin of the oxygen redox activity in layered and cation-disordered Li-excess cathode materials. *Nat. Chem.* **8**, 692–697 (2016).
3. W. E. Gent, K. Lim, Y. Liang, Q. Li, T. Barnes, S.-J. Ahn, K. H. Stone, M. McIntire, J. Hong, J. H. Song, Y. Li, A. Mehta, S. Ermon, T. Tyliszczak, D. Kilcoyne, D. Vine, J.-H. Park, S.-K. Doo, M. F. Toney, W. Yang, D. Prendergast, W. C. Chueh, Coupling between oxygen redox and cation migration explains unusual electrochemistry in lithium-rich layered oxides. *Nat. Commun.* **8**, 2091 (2017).
4. J. Lee, A. Urban, X. Li, D. Su, G. Hautier, G. Ceder, Unlocking the potential of cation-disordered oxides for rechargeable lithium batteries. *Science* **343**, 519–522 (2014).
5. K. Luo, M. R. Roberts, R. Hao, N. Guerrini, D. M. Pickup, Y.-S. Liu, K. Edström, J. Guo, A. V. Chadwick, L. C. Duda, P. G. Bruce, Charge-compensation in *3d*-transition-metal-oxide intercalation cathodes through the generation of localized electron holes on oxygen. *Nat. Chem.* **8**, 684–691 (2016).
6. C. S. Johnson, J.-S. Kim, C. Lefief, N. Li, J. T. Vaughey, M. M. Thackeray, The significance of the Li_2MnO_3 component in 'composite' $xLi_2MnO_3{\cdot}(1-x)LiMn_{0.5}Ni_{0.5}O_2$ electrodes. *Electrochem. commun.* **6**, 1085–1091 (2004).
7. D. Eum, B. Kim, S. J. Kim, H. Park, J. Wu, S.-P. Cho, G. Yoon, M. H. Lee, S.-K. Jung, W. Yang, W. M. Seong, K. Ku, O. Tamwattana, S. K. Park, I. Hwang, K. Kang, Voltage decay and redox asymmetry mitigation by reversible cation migration in lithium-rich layered oxide electrodes. *Nat. Mater.* **19**, 419–427 (2020).
8. R. A. House, G. J. Rees, M. A. Pérez-Osorio, J.-J. Marie, E. Boivin, A. W. Robertson, A. Nag, M. Garcia-Fernandez, K.-J. Zhou, P. G. Bruce, First-cycle voltage hysteresis in Li-rich *3d* cathodes associated with molecular O_2 trapped in the bulk. *Nat. Energy* **5**, 777–785 (2020).
9. D. Mohanty, J. Li, D. P. Abraham, A. Huq, E. A. Payzant, D. L. Wood III, C. Daniel, Unraveling the voltage-fade mechanism in high-energy-density lithium-ion batteries: Origin of the tetrahedral cations for spinel conversion. *Chem. Mater.* **26**, 6272–6280 (2014).
10. J. Hwang, S. Myeong, W. Jin, H. Jang, G. Nam, M. Yoon, S. H. Kim, S. H. Joo, S. K. Kwak, M. G. Kim, J. Cho, Excess-Li localization triggers chemical irreversibility in Li- and Mn-rich layered oxides. *Adv. Mater.* **32**, 2001944 (2020).
11. J. Hwang, S. Myeong, E. Lee, H. Jang, M. Yoon, H. Cha, J. Sung, M. G. Kim, D.-H. Seo, J. Cho, Lattice-oxygen-stabilized Li- and Mn-rich cathodes with sub-micrometer particles by modifying the excess-Li distribution. *Adv. Mater.* **33**, 2100352 (2021).
12. R. A. House, U. Maitra, M. A. Pérez-Osorio, J. G. Lozano, L. Jin, J. W. Somerville, L. C. Duda, A. Nag, A. Walters, K.-J. Zhou, M. R. Roberts, P. G. Bruce, Superstructure control of first-cycle voltage hysteresis in oxygen-redox cathodes. *Nature* **577**, 502–508 (2020).
13. S. Myeong, W. Cho, W. Jin, J. Hwang, M. Yoon, Y. Yoo, G. Nam, H. Jang, J.-G. Han, N.-S. Choi, M. G. Kim, J. Cho, Understanding voltage decay in lithium-excess layered cathode materials through oxygen-centred structural arrangement. *Nat. Commun.* **9**, 3285 (2018).
14. W. Jin, S. Myeong, J. Hwang, H. Jang, J. Sung, Y. Yoo, M. G. Kim, J. Cho, Unraveling the rapid redox behavior of Li-excess 3d-transition metal oxides for high rate capability. *Adv. Energy Mater.* **10**, 1904092 (2020).
15. B. Li, Z. Zhuo, L. Zhang, A. Iadecola, X. Gao, J. Guo, W. Yang, A. V. Morozov, A. M. Abakumov, J.-M. Tarascon, Decoupling the roles of Ni and Co in anionic redox activity of Li-rich NMC cathodes. *Nat. Mater.* **22**, 1370–1379 (2023).
16. D. Luo, H. Zhu, Y. Xia, Z. Yin, Y. Qin, T. Li, Q. Zhang, L. Gu, Y. Peng, J. Zhang, K. M. Wiaderek, Y. Huang, T. Yang, Y. Tang, S. Lan, Y. Ren, W. Lu, C. M. Wolverton, Q. Liu, A Li-rich layered oxide cathode with negligible voltage decay. *Nat. Energy* **8**, 1078–1087 (2023).
17. F. Ning, B. Li, J. Song, Y. Zuo, H. Shang, Z. Zhao, Z. Yu, W. Chu, K. Zhang, G. Feng, X. Wang, D. Xia, Inhibition of oxygen dimerization by local symmetry tuning in Li-rich layered oxides for improved stability. *Nat. Commun.* **11**, 4973 (2020).
18. M. Yoon, Y. Dong, Y. Huang, B. Wang, J. Kim, J.-S. Park, J. Hwang, J. Park, S. J. Kang, J. Cho, J. Li, Eutectic salt-assisted planetary centrifugal deagglomeration for single-crystalline cathode synthesis. *Nat. Energy* **8**, 482–491 (2023).
19. T. Wu, X. Zhang, Y. Wang, N. Zhang, H. Li, Y. Guan, D. Xiao, S. Liu, H. Yu, Gradient "single-crystal" Li-rich cathode materials for high-stable lithium-ion batteries. *Adv. Funct. Mater.* **33**, 2210154 (2023).
20. W. Zeng, F. Liu, J. Yang, B. Zhang, F. Cao, W. Tian, J. Wang, R. Yu, F. Xia, H. Peng, J. Ma, Z. Wang, S. Mu, J. Wu, Single-crystal Li-rich layered cathodes with suppressed voltage decay by double-layer interface engineering. *Energy Storage Mater.* **54**, 651–660 (2023).

21. H. Park, H. Park, K. Song, S. H. Song, S. Kang, K.-H. Ko, D. Eum, Y. Jeon, J. Kim, W. M. Seong, H. Kim, J. Park, K. Kang, In situ multiscale probing of the synthesis of a Ni-rich layered oxide cathode reveals reaction heterogeneity driven by competing kinetic pathways. *Nat. Chem.* **14**, 614–622 (2022).
22. M. Sathiya, G. Rousse, K. Ramesha, C. P. Laisa, H. Vezin, M. T. Sougrati, M.-L. Doublet, D. Foix, D. Gonbeau, W. Walker, A. S. Prakash, M. B. Hassine, L. Dupont, J.-M. Tarascon, Reversible anionic redox chemistry in high-capacity layered-oxide electrodes. *Nat. Mater.* **12**, 827–835 (2013).
23. D. A. Kitchaev, J. Vinckeviciute, A. Van der Ven, Delocalized metal-oxygen π-redox is the origin of anomalous nonhysteretic capacity in Li-ion and Na-ion cathode materials. *J. Am. Chem. Soc.* **143**, 1908–1916 (2021).
24. J.-H. Song, G. Yoon, B. Kim, D. Eum, H. Park, D.-H. Kim, K. Kang, Anionic redox activity regulated by transition metal in lithium-rich layered oxides. *Adv. Energy Mater.* **10**, 2001207 (2020).
25. R. A. House, G. J. Rees, K. McColl, J.-J. Marie, M. Garcia-Fernandez, A. Nag, K.-J. Zhou, S. Cassidy, B. J. Morgan, M. Saiful Islam, P. G. Bruce, Delocalized electron holes on oxygen in a battery cathode. *Nat. Energy* **8**, 351–360 (2023).
26. W. E. Gent, I. I. Abate, W. Yang, L. F. Nazar, W. C. Chueh, Design rules for high-valent redox in intercalation electrodes. *Joule* **4**, 1369–1397 (2020).
27. M. Okubo, A. Yamada, Molecular orbital principles of oxygen-redox battery electrodes. *ACS Appl. Mater. Interfaces* **9**, 36463–36472 (2017).
28. S. Wu, J. Guo, Band gaps and electronic structure of transition-metal compounds. *Sens. Transducers* **159**, 374–378 (2013).
29. M. Saubanère, E. McCalla, J. M. Tarascon, M. L. Doublet, The intriguing question of anionic redox in high-energy density cathodes for Li-ion batteries. *Energy Environ. Sci.* **9**, 984–991 (2016).
30. R. A. House, J.-J. Marie, J. Park, G. J. Rees, S. Agrestini, A. Nag, M. Garcia-Fernandez, K.-J. Zhou, P. G. Bruce, Covalency does not suppress O_2 formation in 4d and 5d Li-rich O-redox cathodes. *Nat. Commun.* **12**, 2975 (2021).
31. M. Ben Yahia, J. Vergnet, M. Saubanère, M.-L. Doublet, Unified picture of anionic redox in Li/Na-ion batteries. *Nat. Mater.* **18**, 496–502 (2019).
32. N. Yabuuchi, K. Yoshii, S. T. Myung, I. Nakai, S. Komaba, Detailed studies of a high-capacity electrode material for rechargeable batteries, Li_2MnO_3-$LiCo_{1/3}Ni_{1/3}O_2$. *J. Am. Chem. Soc.* **133**, 4404–4419 (2011).
33. Y. Xie, M. Saubanère, M.-L. Doublet, Requirements for reversible extra-capacity in Li-rich layered oxides for Li-ion batteries. *Energy Environ. Sci.* **10**, 266–274 (2017).
34. B. Li, R. Shao, H. Yan, L. An, B. Zhang, H. Wei, J. Ma, D. Xia, X. Han, Understanding the stability for Li-rich layered oxide Li_2RuO_3 cathode. *Adv. Funct. Mater.* **26**, 1330–1337 (2016).
35. A. C. W. P. James, J. B. Goodenough, Structure and bonding in lithium ruthenate, Li_2RuO_3. *J. Solid State Chem.* **74**, 287–294 (1988).
36. J. Xu, M. Sun, R. Qiao, S. E. Renfrew, L. Ma, T. Wu, S. Hwang, D. Nordlund, D. Su, K. Amine, J. Lu, B. D. McCloskey, W. Yang, W. Tong, Elucidating anionic oxygen activity in lithium-rich layered oxides. *Nat. Commun.* **9**, 947 (2018).
37. M. G. Kim, C. H. Yo, X-ray absorption spectroscopic study of chemically and electrochemically Li ion extracted Li_y $Co_{0.85}Al_{0.15}O_2$ compounds. *J. Phys. Chem. B* **103**, 6457–6465 (1999).
38. M. G. Kim, H. J. Shin, J.-H. Kim, S.-H. Park, Y.-K. Sun, XAS investigation of inhomogeneous metal-oxygen bond covalency in bulk and surface for charge compensation in Li-ion battery cathode $Li[Ni_{1/3}Co_{1/3}Mn_{1/3}]O_2$ material. *J. Electrochem. Soc.* **152**, A1320 (2005).
39. G. Assat, A. Iadecola, C. Delacourt, R. Dedryvère, J.-M. Tarascon, Decoupling cationic-anionic redox processes in a model Li-rich cathode via *Operando x*-ray absorption spectroscopy. *Chem. Mater.* **29**, 9714–9724 (2017).
40. E. McCalla, A. M. Abakumov, M. Saubanère, D. Foix, E. J. Berg, G. Rousse, M.-L. Doublet, D. Gonbeau, P. Novák, G. Van Tendeloo, R. Dominko, J.-M. Tarascon, Visualization of O-O peroxo-like dimers in high-capacity layered oxides for Li-ion batteries. *Science* **350**, 1516–1521 (2015).
41. W.-S. Yoon, C. P. Grey, M. Balasubramanian, X.-Q. Yang, J. McBreen, In situ x-ray absorption spectroscopic study on $LiNi_{0.5}Mn_{0.5}O_2$ cathode material during electrochemical cycling. *Chem. Mater.* **15**, 3161–3169 (2003).
42. T. Deng, X. Fan, L. Cao, J. Chen, S. Hou, X. Ji, L. Chen, S. Li, X. Zhou, E. Hu, D. Su, X.-Q. Yang, C. Wang, Designing in-situ-formed interphases enables highly reversible cobalt-free $LiNiO_2$ cathode for Li-ion and Li-metal batteries. *Joule* **3**, 2550–2564 (2019).
43. X. Cao, Synthesis and characterization of $LiNi_{1/3}Co_{1/3}Mn_{1/3}O_2$ as cathode materials for Li-ion batteries via an efficacious Sol- Gel method. *Int. J. Electrochem. Sci.* **11**, 5267–5278 (2016).
44. M. Li, J. Lu, Cobalt in lithium-ion batteries. *Science* **367**, 979–980 (2020).
45. J. Jiang, F. Sun, S. Zhou, W. Hu, H. Zhang, J. Dong, Z. Jiang, J. Zhao, J. Li, W. Yan, M. Wang, Atomic-level insight into super-efficient electrocatalytic oxygen evolution on iron and vanadium co-doped nickel (oxy)hydroxide. *Nat. Commun.* **9**, 2885 (2018).
46. N. Zhang, X. Feng, D. Rao, X. Deng, L. Cai, B. Qiu, R. Long, Y. Xiong, Y. Lu, Y. Chai, Lattice oxygen activation enabled by high-valence metal sites for enhanced water oxidation. *Nat. Commun.* **11**, 4066 (2020).
47. S. Ebbinghaus, Z. Hu, A. Reller, Determination of the oxidation states of Cu and Ru in the system $La_{2-x}Sr_xCu_{1-y}Ru_yO_{4-\delta}$ by XANES-measurements. *J. Solid State Chem.* **156**, 194–202 (2001).
48. K. Sardar, E. Petrucco, C. I. Hiley, J. D. B. Sharman, P. P. Wells, A. E. Russell, R. J. Kashtiban, J. Sloan, R. I. Walton, Water-splitting electrocatalysis in acid conditions using ruthenate-iridate pyrochlores. *Angew. Chemie Int. Ed. Engl.* **53**, 10960–10964 (2014).
49. C. I. Hiley, M. R. Lees, J. M. Fisher, D. Thompsett, S. Agrestini, R. I. Smith, R. I. Walton, Ruthenium(V) oxides from low-temperature hydrothermal synthesis. *Angew. Chemie Int. Ed. Engl.* **53**, 4423–4427 (2014).
50. S. G. Minasian, J. M. Keith, E. R. Batista, K. S. Boland, J. A. Bradley, S. R. Daly, S. A. Kozimor, W. W. Lukens, R. L. Martin, D. Nordlund, G. T. Seidler, D. K. Shuh, D. Sokaras, T. Tyliszczak, G. L. Wagner, T.-C. Weng, P. Yang, Covalency in metal–oxygen multiple bonds evaluated using oxygen K-edge spectroscopy and electronic structure theory. *J. Am. Chem. Soc.* **135**, 1864–1871 (2013).
51. F. Frati, M. O. J. Y. Hunault, F. M. F. de Groot, Oxygen K-edge x-ray absorption spectra. *Chem. Rev.* **120**, 4056–4110 (2020).
52. S. Jiao, X. Fu, H. Huang, Descriptors for the evaluation of electrocatalytic reactions: d-band theory and beyond. *Adv. Funct. Mater.* **32**, 2107651 (2022).
53. D. A. Kuznetsov, B. Han, Y. Yu, R. R. Rao, J. Hwang, Y. Román-Leshkov, Y. Shao-Horn, Tuning redox transitions via inductive effect in metal oxides and complexes, and implications in oxygen electrocatalysis. *Joule* **2**, 225–244 (2018).
54. A. K. Padhi, K. S. Nanjundaswamy, C. Masquelier, S. Okada, J. B. Goodenough, Effect of structure on the Fe^{3+} / Fe^{2+} redox couple in iron phosphates. *J. Electrochem. Soc.* **144**, 1609 (1997).
55. J. Reed, G. Ceder, Role of electronic structure in the susceptibility of metastable transition-metal oxide structures to transformation. *Chem. Rev.* **104**, 4513–4534 (2004).
56. D. Eum, B. Kim, J.-H. Song, H. Park, H.-Y. Jang, S. J. Kim, S.-P. Cho, M. H. Lee, J. H. Heo, J. Park, Y. Ko, S. K. Park, J. Kim, K. Oh, D.-H. Kim, S. J. Kang, K. Kang, Coupling structural evolution and oxygen-redox electrochemistry in layered transition metal oxides. *Nat. Mater.* **21**, 664–672 (2022).
57. J. Hong, W. E. Gent, P. Xiao, K. Lim, D.-H. Seo, J. Wu, P. M. Csernica, C. J. Takacs, D. Nordlund, C.-J. Sun, K. H. Stone, D. Passarello, W. Yang, D. Prendergast, G. Ceder, M. F. Toney, W. C. Chueh, Metal–oxygen decoordination stabilizes anion redox in Li-rich oxides. *Nat. Mater.* **18**, 256–265 (2019).
58. K. Ku, B. Kim, S.-K. Jung, Y. Gong, D. Eum, G. Yoon, K.-Y. Park, J. Hong, S.-P. Cho, D.-H. Kim, H. Kim, E. Jeong, L. Gu, K. Kang, A new lithium diffusion model in layered oxides based on asymmetric but reversible transition metal migration. *Energy Environ. Sci.* **13**, 1269–1278 (2020).
59. R. A. House, J.-J. Marie, M. A. Pérez-Osorio, G. J. Rees, E. Boivin, P. G. Bruce, The role of O_2 in O-redox cathodes for Li-ion batteries. *Nat. Energy* **6**, 781–789 (2021).
60. G. Kresse, J. Furthmüller, Efficient iterative schemes for ab initio total-energy calculations using a plane-wave basis set. *Phys. Rev. B* **54**, 11169–11186 (1996).
61. J. P. Perdew, K. Burke, M. Ernzerhof, Generalized gradient approximation made simple. *Phys. Rev. Lett.* **77**, 3865 (1996).
62. X. Li, Y. Qiao, S. Guo, K. Jiang, M. Ishida, H. Zhou, A new type of Li-rich rock-salt oxide $Li_2Ni_{1/3}Ru_{2/3}O_3$ with reversible anionic redox chemistry. *Adv. Mater.* **31**, 1807825 (2019).
63. N. Li, M. Sun, W. H. Kan, Z. Zhuo, S. Hwang, S. E. Renfrew, M. Avdeev, A. Huq, B. D. McCloskey, D. Su, W. Yang, W. Tong, Layered-rocksalt intergrown cathode for high-capacity zero-strain battery operation. *Nat. Commun.* **12**, 2348 (2021).

Acknowledgments: We thank UCRF (UNIST Central Research Facilities) for support of using the equipment. The XANES, EXAFS, and HR-XRD experiments performed at Beamline 9B and 10C of the Pohang Accelerator Laboratory were supported in part by the MSIT and POSTECH. **Funding:** This work was supported by National Research Foundation of Korea (NRF) (RS-2024-00428511, RS-2024-00451160, RS-2024-00435493, and RS-2023-00208929), Regional Innovation Strategy (RIS) through the NRF funded by the Ministry of Education (MOE) (2021RIS-003), National Research Council of Science and Technology (NST) (no. GTL24011-102), and The Supercomputing Center/Korea Institute of Science and Technology Information with supercomputing resources including technical support (KSC-2024-CRE-0463 to H.-W.L.). **Author contributions:** Conceptualization: M.-H.K., H.J., and H.-W.L. Methodology: M.-H.K., D.-H.S., and H.-W.L. Investigation: M.-H.K., H.J., E.L., J.S., J.P., A.C., T.K., M.C., E.K., Y.H.J., and S.J.K. Visualization: M.-H.K., H.J., and E.L. Funding acquisition: M.G.K., D.-H.S., and H.-W.L. Supervision: S.J.K., J.C., Y.L., M.G.K., D.-H.S., and H.-W.L. Writing—original draft: M.-H.K. Writing—review and editing: H.J., E.L., Y.L., D.-H.S., and H.-W.L. **Competing interests:** The authors declare that they have no competing interests. **Data and materials availability:** All data needed to evaluate the conclusions in the paper are present in the paper and/or the Supplementary Materials.

Submitted 8 September 2024
Accepted 17 January 2025
Published 19 February 2025
10.1126/sciadv.adt0232